



Probing the Gas-Phase Dynamics of Graphene Chemical Vapour Deposition using *in-situ* UV Absorption Spectroscopy

Shivayogimath, Abhay; Mackenzie, David; Luo, Birong; Hansen, Ole; Bøggild, Peter; Booth, Tim

Published in:
Scientific Reports

Link to article, DOI:
[10.1038/s41598-017-06276-y](https://doi.org/10.1038/s41598-017-06276-y)

Publication date:
2017

Document Version
Publisher's PDF, also known as Version of record

[Link back to DTU Orbit](#)

Citation (APA):
Shivayogimath, A., Mackenzie, D., Luo, B., Hansen, O., Bøggild, P., & Booth, T. (2017). Probing the Gas-Phase Dynamics of Graphene Chemical Vapour Deposition using *in-situ* UV Absorption Spectroscopy. *Scientific Reports*, 7(1). <https://doi.org/10.1038/s41598-017-06276-y>

General rights

Copyright and moral rights for the publications made accessible in the public portal are retained by the authors and/or other copyright owners and it is a condition of accessing publications that users recognise and abide by the legal requirements associated with these rights.

- Users may download and print one copy of any publication from the public portal for the purpose of private study or research.
- You may not further distribute the material or use it for any profit-making activity or commercial gain
- You may freely distribute the URL identifying the publication in the public portal

If you believe that this document breaches copyright please contact us providing details, and we will remove access to the work immediately and investigate your claim.

SCIENTIFIC REPORTS



OPEN

Probing the Gas-Phase Dynamics of Graphene Chemical Vapour Deposition using *in-situ* UV Absorption Spectroscopy

Abhay Shivayogimath¹, David Mackenzie¹, Birong Luo¹, Ole Hansen¹, Peter Bøggild^{1,2} & Timothy J. Booth^{1,2}

The processes governing multilayer nucleation in the chemical vapour deposition (CVD) of graphene are important for obtaining high-quality monolayer sheets, but remain poorly understood. Here we show that higher-order carbon species in the gas-phase play a major role in multilayer nucleation, through the use of *in-situ* ultraviolet (UV) absorption spectroscopy. These species are the volatilized products of reactions between hydrogen and carbon contaminants that have backstreamed into the reaction chamber from downstream system components. Consequently, we observe a dramatic suppression of multilayer nucleation when backstreaming is suppressed. These results point to an important and previously undescribed mechanism for multilayer nucleation, wherein higher-order gas-phase carbon species play an integral role. Our work highlights the importance of gas-phase dynamics in understanding the overall mechanism of graphene growth.

Large-area, high quality monolayer graphene suitable for applications in flexible electronics can now be reproducibly obtained by chemical vapour deposition (CVD) of graphene on copper, thanks to extensive research into understanding its growth process over the past years^{1–5}. It is generally agreed that the growth process begins with an influx of carbon precursors onto the copper surface, which leads to a local supersaturation of active carbon species and triggers the nucleation of graphene domains^{6,7}. The growth of these nascent nuclei depletes the carbon concentration in their vicinity, which suppresses further nucleation^{7,8}. The nuclei continue to expand and eventually coalesce to form extended sheets that span the entire surface of the substrate. Due to the limited solubility of carbon in copper, the reaction is surface-limited, thereby providing a high selectivity towards monolayer growth⁹. The dynamics of the growth process are influenced by four key parameters: temperature, pressure, methane (CH₄) concentration, and hydrogen (H₂) concentration. The effects of temperature are well-understood: higher temperatures generally lead to higher quality films by improving the mobility and adsorption-desorption kinetics of surface-bound carbon, thereby improving the grain crystal quality^{7,8}. The system pressure and flowrates govern the mass transport¹⁰ and residence time of the gases in the chamber¹¹, as well as the surface dynamics of the copper substrate on account of copper sublimation at reduced pressures^{12,13}. The effects of varying the methane and hydrogen partial pressures are closely intertwined with the system pressure, with low CH₄/H₂ and high CH₄/H₂ ratios favouring monolayer growths in the atmospheric pressure and low pressure regimes, respectively^{6,10,13–16}. The partial pressures of the gases also determine the chemical potential for carbon deposition, and hence the kinetics of graphene growth on the copper surface. A higher methane partial pressure increases the chemical potential, shifting the graphene grain morphology towards diffusion-limited dendritic growth, whereas hydrogen reduces the potential, favouring kinetically-limited growth of hexagonal domains at high partial pressures^{3,17–23}.

However, certain aspects of the role of hydrogen still remain unclear. In particular, while a large hydrogen partial pressure is crucial for obtaining high-quality, hexagonal domains, several studies have reported an increase in multilayer nucleation under such conditions^{16,23–26}. These observations have so far been explained

¹DTU Nanotech, Technical University of Denmark, Ørsteds Plads, 345E, Kongens Lyngby, 2800, Denmark. ²Centre for Nanostructured Graphene (CNG), Technical University of Denmark, Ørsteds Plads, 345C, Kongens Lyngby, 2800, Denmark. Correspondence and requests for materials should be addressed to T.J.B. (email: tim.booth@nanotech.dtu.dk)

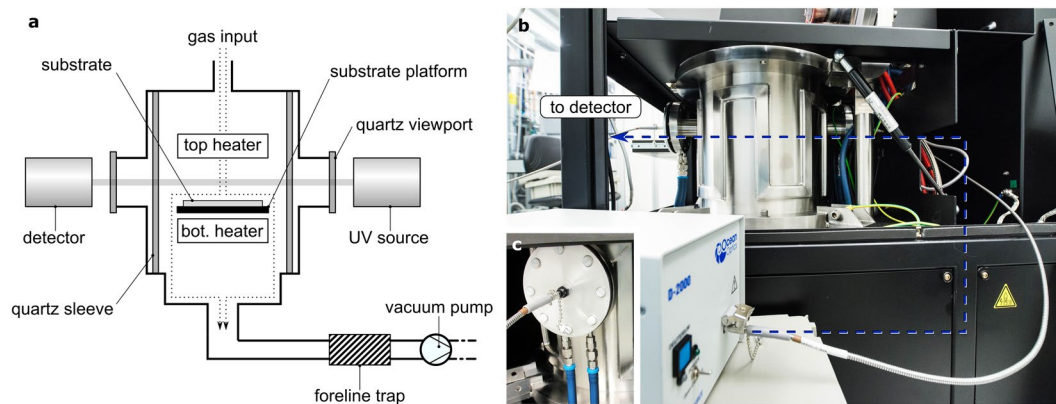


Figure 1. Illustration of the experimental setup. (a) schematic of the experimental setup, where a UV spectrometer is mounted on the cold wall CVD system so as to monitor the composition of the gases in the region directly above the copper catalyst layer; (b,c) photographs of the experimental setup; (b) fiber optic cables transmit light (blue dashed line) to and from the detector and UV lamp through the reaction chamber; the cables are attached to collimating lenses, which are firmly and precisely mounted onto the (c) front and back viewports.

by hydrogenation of the domain edges, which decouples them from the copper surface and allows diffusion of carbon species underneath the initial monolayer^{22, 27, 28}.

Here, through the use of a novel *in-situ* gas-phase ultraviolet (UV) absorption spectroscopic technique, we provide evidence for an alternate, possibly complementary explanation, wherein large concentrations of hydrogen activate carbon contaminants in the reaction chamber, volatilizing them and making them available for nucleation. These contaminants, which comprise oils, greases, and condensed products of pyrolysis, accumulate in the chamber as a result of backstreaming from downstream system components, such as the exhaust lines, the vacuum pump, and the foreline trap. The resultant cracking of these species by hydrogen at high temperatures produces the necessary gas-phase precursors for multilayer nucleation. A dramatic reduction in multilayer nucleation is consequently achieved by suppressing backstreaming in a cleaned reaction chamber, which strongly supports this interpretation. The results thus demonstrate that multilayer nucleation can in some cases be wholly ascribed to the volatilized products of reactions between backstreamed contaminants and H₂, highlighting the importance of the role of gas-phase carbon species in multilayer nucleation.

Results

***In-situ* UV spectroscopic measurements.** *In-situ* UV absorption spectroscopy measurements were conducted in a cold-wall CVD system according to Fig. 1. Spectral measurements were continuously recorded from the end of the annealing phase to the end of the growth phase, and the absorbance at each time interval was calculated using the first spectrum in the series as the reference (see Methods). The layout of the system provides direct optical access to the gas directly above the growth substrate. The choice of UV absorption spectroscopy over more conventional infrared and laser-based spectroscopic methods (e.g. - FTIR, coherent anti-stokes Raman spectroscopy, laser-induced fluorescence spectroscopy, cavity ring-down spectroscopy) was made for several reasons. The large infrared background noise from the graphite heaters at typical growth temperatures precludes the use of infrared spectroscopy²⁹, whereas laser-based methods run the risk of inducing photochemical reactions and producing spurious results at high temperatures. In contrast, UV absorption spectroscopy is a simple, non-invasive, and sensitive tool that provides direct, real-time measurements of changes in concentrations of photoactive species and is limited largely by instrumental noise³⁰.

***In-situ* spectroscopy and characterization of a standard growth process.** Figure 2 shows the absorption spectra and characterization results of a typical growth on copper foil at 1020 °C, 20 mbar, 1 sccm CH₄ and 1000 sccm H₂ flow. High-purity copper foils were fabricated in-house in order to minimize impurities and surface imperfections, which could otherwise adversely influence our results³¹ (see Methods). The sample was annealed at growth temperature in 700 sccm argon (Ar) flow for 30 minutes, after which Ar was turned off and H₂ was introduced. Following a stabilization period of 90 seconds, the growth phase was executed for 30 seconds by introducing CH₄.

The addition of hydrogen after 60 seconds is accompanied by an abrupt overall increase in the absorbance, followed by a decrease in the absorbance in two broad bands around 220 nm and 256 nm (Fig. 2a,b) that eventually become negative after approximately 25 seconds. In addition, the 220 nm peak decreases faster than the 256 nm peak. The introduction of CH₄ after 150 seconds has a negligible effect on the absorption spectrum. Subsequent scanning electron microscopy (SEM) of the copper surface after growth (Fig. 2c) indicates that the graphene grains are monolayers with multilayer regions near the centre of individual domains. Micro-Raman maps (Fig. 2d,e) show I(2D)/I(G) ≈ 2 and I(D)/I(G) ≈ 0 in the peripheral regions of the grain, indicating the presence of defect-free monolayer graphene, and I(2D)/I(G) < 1 and I(D)/I(G) > 0 in the centre of the grain, indicating the presence of a mixture of multi-layered and defective graphene. Some of the grains in Fig. 2c display a hexagonal morphology; however the larger grains are predominantly rounded or irregular with multilayer

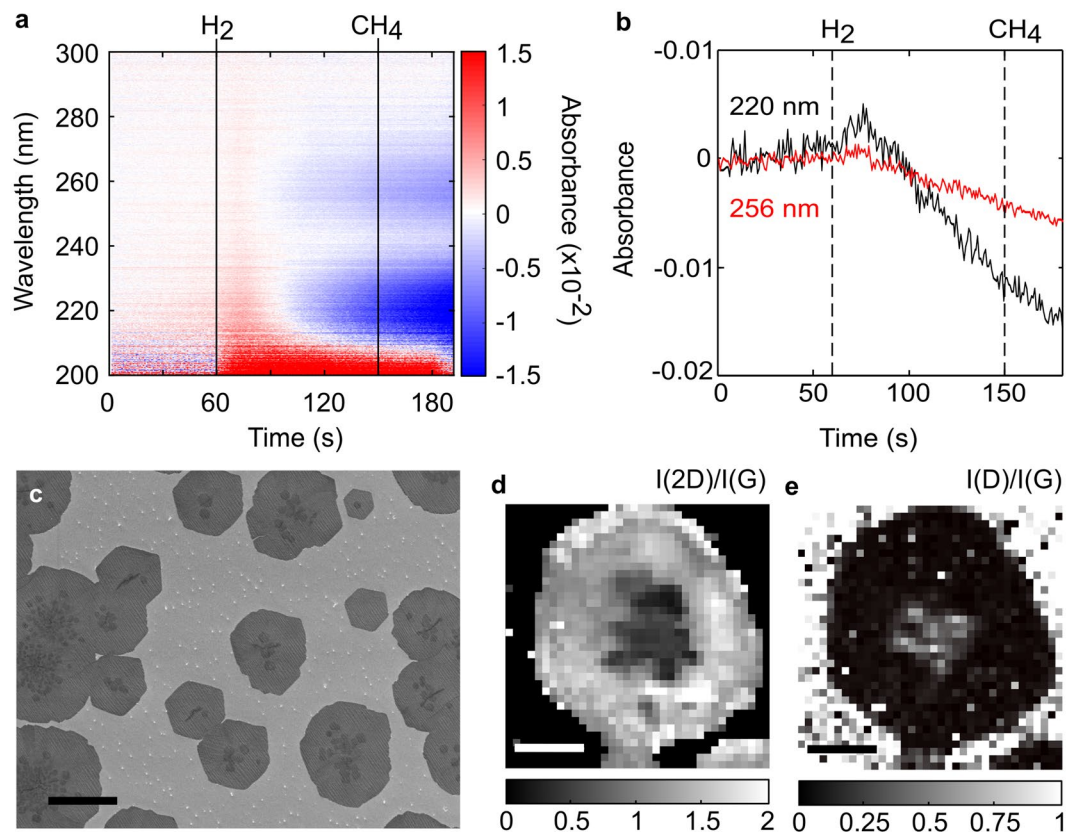


Figure 2. *In-situ* UV absorption spectroscopy and characterization of a standard CVD growth. (a) Time evolution of the absorbance spectra and (b) line profiles of the 220 nm (black) and 256 nm absorption peaks (red), with the dotted lines at 60 s and 150 s denoting when H₂ and CH₄ are introduced, respectively. (c) SEM image of the corresponding growth (scale bar 10 μm). (d,e) Raman maps of a single graphene grain on copper (d) I(2D)/I(G) ratio and (e) I(D)/I(G) ratio. Scale bars in (d) and (e) are 5 μm.

patches. Moreover, multilayer patches are associated with rounded/irregular grain boundaries in the image, while grains with limited multilayer growth appear more hexagonal.

Control measurements of the absorption of source gases. Control measurements of the room temperature absorbance spectra of all source gases, recorded in the absence of a copper substrate in the chamber, show no measurable absorbance relative to vacuum in the spectral regions of interest (Supplementary Fig. 1), confirming that neither the source gases nor any impurities present are responsible for the observed absorption (at least at room temperature). High temperature absorbance measurements of Ar and H₂ are presented in Fig. 3, and were also recorded in the absence of a copper substrate in the chamber. Prior to adding Ar or H₂, an initial increase in absorbance at 220 nm (and to a lesser extent at 256 nm) is observed while the chamber is still in vacuum. Adding argon results in a mild increase in absorption across the spectrum (Fig. 3a,b), but in the case of hydrogen the absorption increases initially, and then drops in the same 220 nm and 256 nm spectral regions (Fig. 3c,d) as seen in the standard growth recipe (Fig. 2a). As such, we attribute the absorption behaviour observed in standard growth recipe entirely to the effects of hydrogen at high temperatures.

The Beer-Lambert law states that the absorbance A_i due to an absorbing species i is proportional to its concentration c_i , its absorption coefficient ϵ_i , and the optical path length l :

$$A_i = \epsilon_i c_i l \quad (1)$$

Changes in absorbance can thus be directly ascribed to changes in concentration of the absorbing species in this experiment. Moreover, a negative absorbance implies that the concentration of said species is lower than when the reference spectrum was recorded.

Our observations therefore suggest that absorbing species accumulate within the chamber when the system is in vacuum, and are gradually removed when hydrogen is introduced. The species responsible for absorption at 220 nm are removed faster than those responsible for the 256 nm absorption. Pressurization of the chamber with argon stabilizes the concentration of said species. Additional experiments where the chamber was cyclically filled with hydrogen and pumped down to vacuum demonstrated the same behaviours, and also resulted in an improvement in base pressure from 0.05 mbar prior to the first hydrogen cycle to 0.038 mbar after the final hydrogen cycle (Supplementary Fig. 2). Moreover, some of the spectral attenuations in vacuum survived

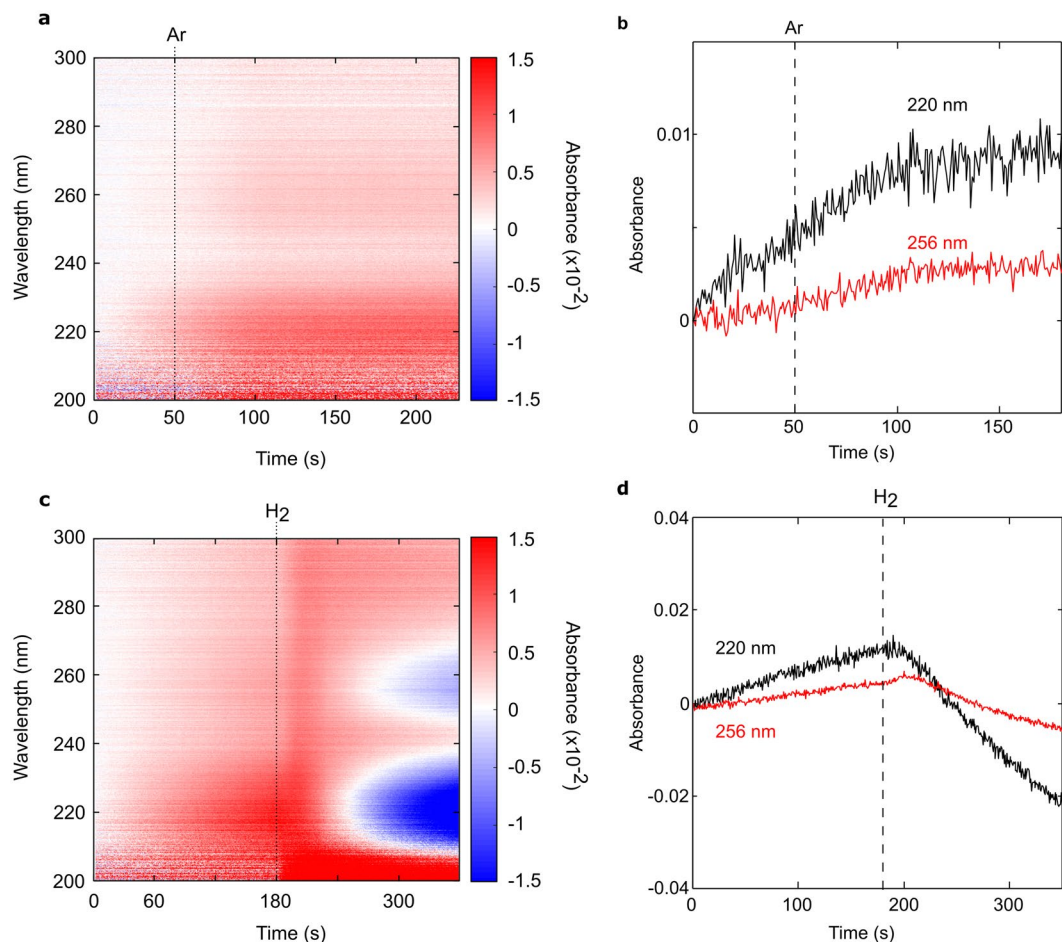


Figure 3. Absorbance spectra of pure argon and hydrogen at growth temperatures. (a) Time evolution of the absorbance and (b) line profiles of the 220 nm and 256 nm peaks for hydrogen, where the dotted line at 50 s denotes when hydrogen is added in vacuum; (c) Time evolution of the absorbance and (d) line profiles of the 220 nm and 256 nm peaks for Argon, where the line at 180 s denotes when argon is added in vacuum.

upon cooldown to room temperature, but were reversed upon manually cleaning the quartz walls of the reactor (Supplementary Fig. 3). These results cumulatively suggest that hydrogen cleans the chamber of contaminants, which are subsequently re-introduced and accumulate in the chamber when the system is pumped down to vacuum. The contaminants therefore most likely originate from downstream systems components, and diffuse back into the chamber during pumping.

Absorption measurements of H₂ and Ar post-cleaning. In light of these findings, we repeated our high temperature Ar and H₂ absorption control experiments (Fig. 4) after the chamber and downstream components were thoroughly cleaned and/or replaced with new components (see Methods). Introducing Ar (Fig. 4a,b) or H₂ (Fig. 4c,d) into the chamber now results in a largely uniform attenuation of the spectrum, with no negative absorption peaks previously observed for hydrogen. A broad absorption below 260 nm is now observed in the hydrogen control experiment (Fig. 4c).

***In-situ* spectroscopy and characterization of a standard growth process post-cleaning.** Repeating the growth recipe in Fig. 2 after cleaning of the chamber results in a dramatic change in the absorption spectra and graphene produced (Fig. 5). Negative absorbance peaks are no longer observed when hydrogen is introduced (Fig. 5a,b), and we see a dramatic reduction in multilayer nucleation (Fig. 5c–e) and an increased, more homogeneous monolayer nucleation density. The large I(D)/I(G) ratio in Fig. 5e is in accordance with the large number of edges in the incompletely grown graphene layer. We note that the nucleation density has increased dramatically in this case; we attribute this to the fact that while the exact same recipe was used in both cases, the measured temperature in the reaction zone was ~20–30 °C lower than before. This is likely the result of a change in the thermal reflection characteristics of the chamber upon removal of copper deposits from the chamber surfaces during cleaning. However, we do not expect this to have adversely influenced our findings, since a lower temperature should have increased the occurrence of multilayered nuclei, as reported previously in literature³², not reduced it as it has here.

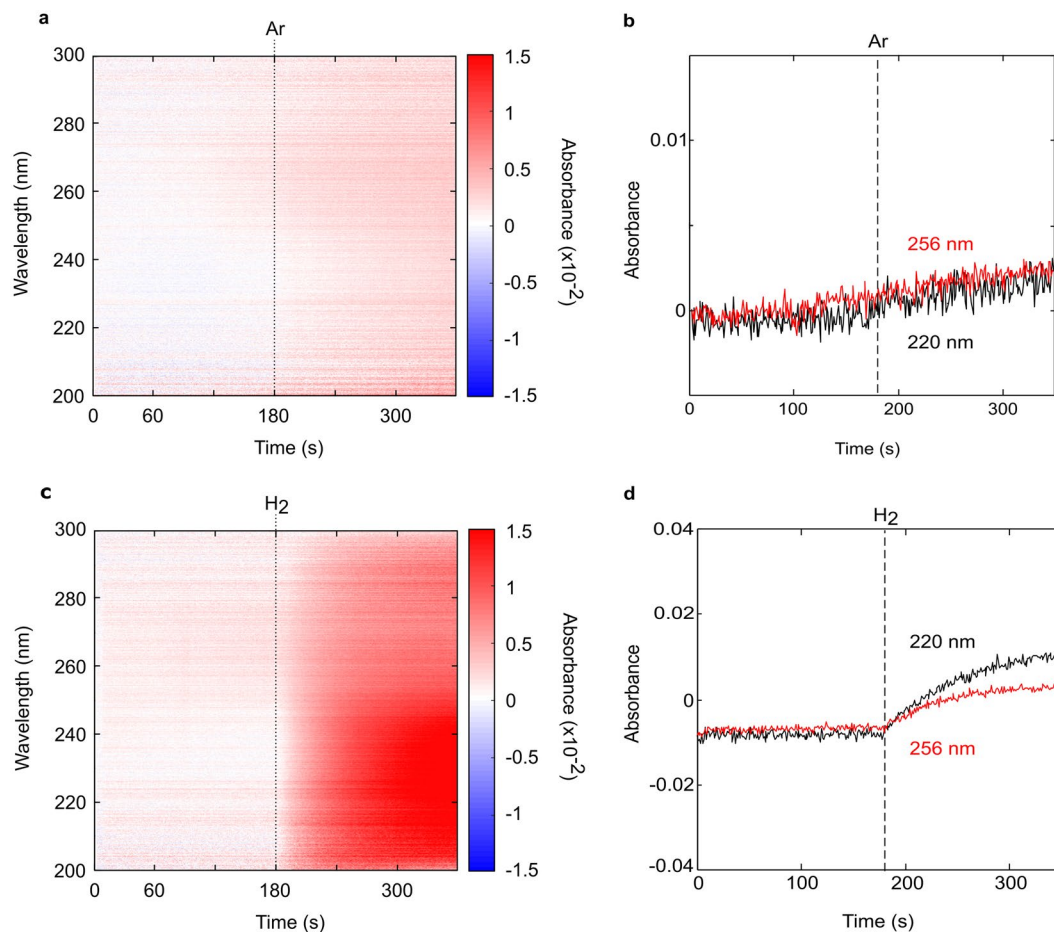


Figure 4. High temperature absorbance spectra of argon and hydrogen post-cleaning. **(a)** Time evolution of the absorbance and **(b)** line profiles of the 220 nm and 256 nm peaks for hydrogen; **(c)** Time evolution of the absorbance and **(d)** line profiles of the 220 nm and 256 nm peaks for Argon. Lines at 180 s denote when the respective gases are added in vacuum.

Characterization of surface contaminants during growth. Figure 6 illustrates the results of repeating the standard growth recipe before chamber cleaning in the absence of methane. White particles with dendritic edges are dispersed across the entire copper surface (Fig. 6a,b) with surface distributions that closely resemble graphene nucleation patterns from similar growths (Fig. 6c). X-ray photoelectron spectroscopy (XPS) of the copper surface before and after growth (Fig. 6d) shows an increase in the carbon concentration and the appearance of fluorine compounds after growth. The C1s spectrum (Fig. 6e) shows, in addition to adventitious carbon, two peaks at 291.3 eV and 293.7 eV. The F1s spectrum (Fig. 6f) shows a clear peak at 688.9 eV that is characteristic of fluorocarbon compounds. While higher energy peaks in the C1s region are more typically associated with plasmon loss features, the fact that graphene should not be present on the surface in this case and that organic fluorine signatures are clearly evident in the F1s region leads us to ascribe the 291.3 eV and 293.7 eV peaks to fluorocarbons instead. Moreover, the peaks correspond closely to the 291.4 eV and 293.8 eV peaks seen for Fomblin³³, a commonly used perfluoropolyether (PFPE) grease in vacuum pumps, and one that was also present in our pump. We note that organic fluorine compounds are an unusual contaminant to find in electroplated foils inside a cleanroom; while PTFE containers have previously³⁴ been suggested as a potential fluorocarbon source, we used polypropylene wafer trays in our experiments, which precludes this as a possibility. The results therefore suggest that the contaminants are introduced during the growth process from the chamber itself, and originate from downstream components such as the pump. Moreover, the striking resemblance between the contaminant distribution and graphene nucleation patterns in Fig. 6a–c indicates that the contaminants were present during the growth phase and actively contributed to nucleation.

Discussion

Based on our observations, we ascribe the nucleation of multilayers to the products of the reactions of hydrogen with backstreamed carbon contaminants from downstream system components. Backstreaming is a well-known issue affecting vacuum systems, and is especially relevant when operating at low pressures, for extended periods of time, and when using oil pumps^{35–40}. Whilst oil-based vacuum pumps can be fitted with oil traps to mitigate backstreaming, a finite amount of backstreaming is almost always present, and the traps themselves can easily be exhausted without regular maintenance^{35, 41}. While the results here have been demonstrated for a cold-wall

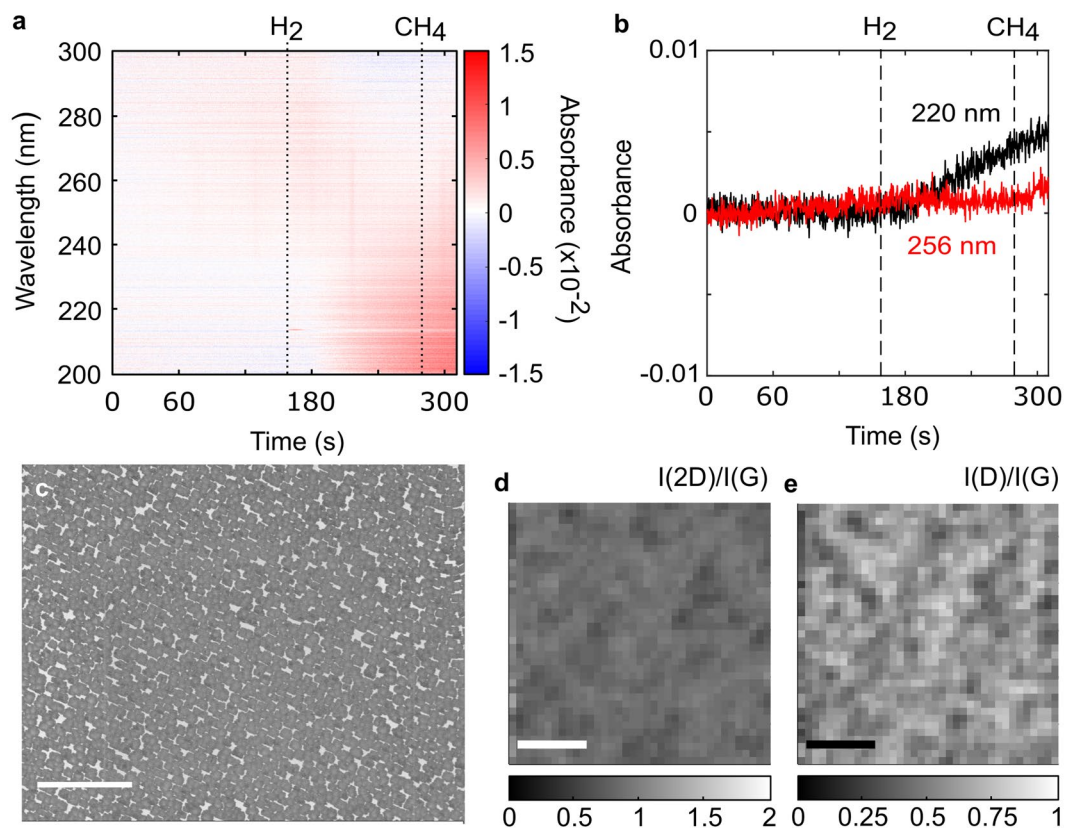


Figure 5. Absorption measurements and characterization of a standard CVD growth when backstreaming is suppressed. **(a)** Time evolution of the absorbance spectra and **(b)** line profiles of the 220 nm (black) and 256 nm absorption peaks (red), with the dotted lines at 158 s and 279 s denoting when H₂ and CH₄ are introduced, respectively. **(c)** SEM image of the corresponding growth (scale bar 10 μ m). **(d,e)** Raman maps of a single graphene grain on copper **(d)** I(2D)/I(G) ratio and **(e)** I(D)/I(G) ratio. Scale bars in **(d)** and **(e)** are 5 μ m.

system, similar effects are expected for a hot-wall furnace that is continuously pumped during operation or standby, because pumping at low pressures continuously introduces backstreamed carbon into the chamber (Supplementary Fig. 3). Similarly, while primarily affecting low pressure growths, backstreaming can also affect atmospheric pressure growths if the system is kept in vacuum at room temperature for extended periods of time (Supplementary Fig. 4). Carbon contaminants can also be introduced to the system through other routes and even where dry pumps are employed⁴¹, such as the condensation in the pumping lines of higher-order hydrocarbons produced during CVD reactions⁴⁰. In such cases, backstreaming also poses a potential issue for dry pumping and turbomolecular pumping systems.

The exact chemical composition of the contaminants is still under investigation; the differences in the rates of change in the 220 nm and 256 nm absorbance peaks suggest that more than one species is likely involved. However, the exact chemical identities and concentrations of the species cannot be determined solely from UV absorption data due to numerous reasons: (1) there is very limited literature on UV absorption spectra of species at elevated temperatures with which to benchmark our results, (2) UV absorbance of most species is temperature-dependant, precluding the use of room temperature data for analysis, (3) the measured absorbance is a convolution of absorption by multiple species, which makes accurate quantification difficult. As such, a more quantitative technique would be needed to identify the species responsible. Nevertheless, it is well-known that backstreaming contaminants are primarily composed of vapours or degraded fragments of pump oils and greases; these comprise a wide range of lubricants used in vacuum systems, such as fluorocarbons, silicones, olefins, esters, and ethers^{36,39}.

While the XPS results in Fig. 6 certainly implicate fluorocarbons as the culprit, the exact composition of contaminants is likely to be more complex and variable, as the type and concentration of backstreamed species depends strongly on the specifics of the growth system and its operational history^{35,37,38}. As such, the composition can vary from system to system, and even between runs on the same system. This variability can, for instance, be seen when comparing the hydrogen spectra of Figs 2, 3, 4, and Supplementary Fig. 2. Furthermore, previous reports in literature on hydrogen etching of the quartz walls and subsequent formation SiO_x impurities⁴² could equally be explained by backstreaming of silicone-based greases. As such, it is unlikely that a single species plays a dominant role in multilayer nucleation in all cases, but rather a plethora of species that can collectively be categorized as higher-order carbon contaminants.

Backstreamed contaminants may nucleate multilayers by providing an impurity site that locally lowers the chemical potential for graphene growth^{43,44}, but in light of the fact that these are carbonaceous contaminants,

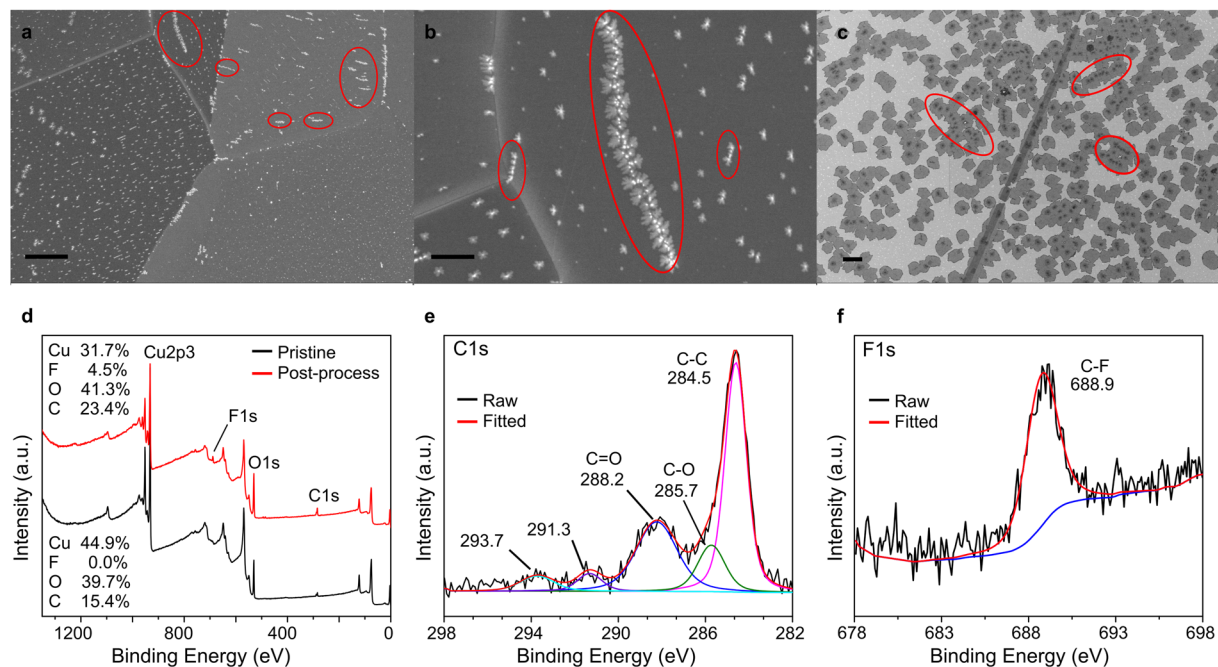


Figure 6. SEM and XPS characterization of a standard CVD growth without methane. **(a,b)** SEM images of the copper surface post-growth, showing the morphology of surface contaminants (red circles; scale bars 10 μm and 2 μm , respectively). **(c)** SEM image of a typical growth for comparison, with the highlighted circles showing the morphological similarities between the surface contaminants in **(a)** and **(b)** and the nucleation patterns in **(c)**. Scale bar 10 μm . **(d,f)** XPS spectra of **(d)** the copper surface before and after growth, with surface elemental compositions indicated for each case (in atomic percent), and of the corresponding **(e)** carbon and **(f)** fluorine signatures.

we believe our results support a novel explanation for the mechanism of the formation of multilayers during the CVD growth of graphene: hydrogen-induced cracking, volatilization and subsequent deposition of higher-order carbon contaminants onto the copper surface presents a large, instantaneous flux of carbon that triggers premature local supersaturation and simultaneous nucleation of multiple layers. The rapid nucleation and growth that such a large initial carbon flux would furnish would also result in the formation and encapsulation of defective multilayers and residual amorphous carbon at the centre of graphene domains, which we observe via Raman spectroscopic maps (Fig. 2d,e), and a shift from attachment-limited hexagonal growth to diffusion-limited growth of irregular grain boundaries, which we observe via SEM (Fig. 2c). While the broader question of the role of higher-order carbon species present in the gas-phase in multilayer nucleation is the topic of several recent theoretical studies^{11, 45–47} and requires further experimental confirmation, our results provide compelling evidence to suggest that the deposition of higher-order carbonaceous species onto the catalyst surface contributes significantly to multilayer nucleation.

Beyond the initial nucleation, the ultimate size of the secondary graphene layers would be governed by the carbon diffusion length and the rate at which the primary monolayer expands. In principle, growth of multilayers could be sustained through the modulation of the carbon chemical potential (i.e., H_2 and CH_4 flow rates), such that the initial monolayer grows fast enough to prevent depletion of excess carbon from the nucleation point (and hence suppress adlayer nucleation), but not so fast that it encapsulates and stunts the growth of the secondary layers. Indeed, this ‘sweet spot’ for CH_4/H_2 flowrates has been demonstrated by several studies^{20, 23, 24, 48}.

It is important to note at this stage that the absorbance values reported here represent extremely low concentrations of contaminants (on the order of ppm concentrations). As such, the contaminants themselves do not provide sufficient carbon chemical potential to nucleate and sustain the growth of graphene in the absence of methane¹⁸, which explains why no graphene domains were seen when repeating the growth without methane (Fig. 6).

In conclusion, we have used a novel *in-situ* spectroscopic tool to probe the effect of gas-phase dynamics on the CVD growth of graphene, and have found that carbonaceous contamination introduced into the chamber through vacuum backstreaming plays a key role in multilayer nucleation. This holds important implications for both research into graphene growth dynamics and the large-scale manufacture of graphene⁵, where continuous operation is required, and where oil pumps are frequently used. Moreover, the findings here are also applicable to dry pumping CVD systems, where pyrolytic products have accumulated in downstream components through continuous use, and to atmospheric pressure systems, where the chamber is continuously pumped down while in standby. As such, modifications in operating procedures should be considered to ensure that backstreaming and general carbon contamination in the chamber are minimized. For instance, switching from wet pumping systems to dry pumps, regular maintenance and cleaning of downstream and chamber components (and

cleaning components in furnaces), reducing pumping times when there is no gas flow, and operating at atmospheric pressures during standby and operation modes are potential steps that can be taken to mitigate the effects of backstreaming.

More importantly, the findings presented here address the commonly reported observation that the presence of large hydrogen concentrations during graphene CVD, and in particular during low pressure growths, induce multilayer nucleation. In a broader perspective, the results also point to an unexplored route by which multilayer nucleation may be initiated, where the presence of higher-order carbon species in the gas-phase induce premature local supersaturation and nucleation of multilayered domains. Finally, gas-phase UV absorption spectroscopy proves to be a non-invasive and sensitive tool for the *in-situ* study of gas-phase dynamics on graphene growth. In light of its relevance towards preventing multilayer nucleation and monitoring backstreaming in real-time, this method may prove to be a scalable and versatile process monitoring tool for large-scale graphene CVD systems, and for vacuum systems in general where backstreaming poses a potential concern.

Methods

Copper substrate preparation. To mitigate the effects of rolling lines and impurities associated with commercial foils, high-purity electroplated copper substrates were fabricated in-house. A thin layer (100 nm) of copper strike layer was sputtered (Lesker, 99.999%) onto RCA-cleaned SiO₂ wafers in a cleanroom facility. 30 μm of copper was subsequently electroplated onto the strike layer in an acidic electroplating bath consisting of 94 g/L CuSO₄·5H₂O (Sigma Aldrich, ≥98.0%) and 100 ml/L H₂SO₄ (Merck, 95–97%). Copper electroplating in a sulfuric acid bath is highly selective towards copper deposition, but nevertheless, low current density DC plating was employed to avoid co-deposition of potential impurities from the solution. The plated films were thoroughly rinsed in deionized water and dried with a combination of acetone and isopropanol rinsing and blow-drying under N₂ flow. Finally, the foils were delaminated from the SiO₂ wafer immediately before inserting them into the growth chamber, revealing an atomically flat surface (Supplementary Fig. 5), onto which our growths were subsequently carried out^{17, 49, 50}.

***In-situ* UV absorption spectroscopy.** Growth and spectroscopic measurements were conducted using an Aixtron Black Magic cold-wall CVD system situated inside a cleanroom. Figure 1a provides a schematic illustration of the experimental setup. Source gases (Ar, H₂, CH₄) are introduced into the chamber via a showerhead assembly, whereby the gases flow past the top heater and heater sample stage, eventually exiting the chamber via the gas outlets at the bottom of the reactor. The reactor uses a rotary vane oil pump (Leybold) and a sorbent fore-line trap filled with alumina beads. Two quartz viewports, situated 180° from one another, provide optical access to the chamber (Fig. 1a,b). The optical path length between the two viewports is 80 cm. A deuterium lamp source (Ocean Optics D-2000-S-DUV) transmits deep UV light at an intensity of 3 mW/cm² through one of the viewports (Fig. 1b), and a spectrometer (Ocean Optics QEPro) with a CCD detector tuned to a wavelength range of 200–300 nm collects the transmitted light via the other viewport (Fig. 1b,c). The viewports and the quartz sleeve were replaced with UV-grade quartz for all measurements. Both the light source and the detector are coupled to solarisation-resistant fibre optic cables and UV-grade collimating lenses to project and collect light from the chamber, respectively. The beam is approximately 2 cm above the substrate platform.

A series of transmission spectra are continuously recorded from 1–3 minutes before the end of the annealing phase until the end of the growth phase. All spectra are acquired in single acquisition mode with the same integration time. The integration time was adjusted to be in the range of 800–1000 ms prior to each experiment to obtain the maximum transmitted signal at room temperature while the system is at base pressure. A dark spectrum is taken shortly before the continuous recording, which is then subtracted from all subsequent spectra. The initial spectrum in the spectral series is used as the reference spectrum. Absorption spectra are subsequently calculated for each spectrum in the series using the equation below:

$$A = \log_{10} \left(\frac{I_{0,k}}{I_{i,k}} \right) \quad (2)$$

where $I_{0,k}$ and $I_{i,k}$ are the spectral intensities of reference spectrum (in this case the initial spectrum intensity) and the i^{th} spectrum, respectively, for a given wavelength, k . A series of absorption spectra is thus obtained, with the time interval between spectra defined by the integration time for the experiment.

Graphene growth. CVD growth of graphene was performed in the Aixtron Black Magic cold-wall CVD system as follows: A small piece of copper foil is placed at the centre of the substrate platform. The chamber is subsequently pumped to base pressure (0.03 mbar for 10 minutes) and flushed with argon (99.9995%, AGA) three times before being pumped down to base pressure for 10 minutes again. The chamber is then pressurized to 20 mbar with argon and heated to 1000 °C (with both the top and bottom graphite heaters on) under 700 sccm argon flow. The copper foil is annealed for 30 minutes at temperature, after which 1000 sccm H₂ is added. After 2 minutes, once the gas flow has stabilized, 1 sccm CH₄ (99.9995%, AGA) is added for 30 seconds. The sample is subsequently cooled down under 1000 sccm Argon flow.

Cleaning of the chamber and downstream components. The chamber was cleaned by disassembling and manually cleaning individual components or replacing them with new ones. Quartz components were replaced with new ones, or were cleaned in a copper etchant solution and annealed in a furnace at 1200 °C to burn off carbon contaminants. Finally, the chamber was heated to 550 °C and an air plasma generated for 15 minutes to burn off any remaining carbon contaminants. This procedure was found to be effective at removing contamination from the system, as judged by spectroscopic measurements (Supplementary Fig. 6). The downstream

components were cleaned as follows: the pump was replaced with a new one, the pump hose and filters were cleaned, and the foreline trap was refilled with new alumina sorbent beads.

Sample characterization. Scanning electron microscopy (SEM) was conducted with a Zeiss LEO 1550 at 5.00 keV. Raman micro-mapping was performed with a Thermo Fisher DXR microscope (455 nm, 6 mW, 10 s × 3 exposure time, 100× objective, 500 nm step size). X-ray photoelectron spectroscopy (XPS) measurements were performed with a Thermo Fisher Scientific K-alpha XPS system using a Al K α X-ray source (1486.7 eV).

Data availability. The data that support the findings of this study are available from the corresponding author upon request.

References

1. Wu, T. *et al.* Fast growth of inch-sized single-crystalline graphene from a controlled single nucleus on Cu – Ni alloys. *Nat. Mater.* **15**, 43–48 (2016).
2. Hao, Y. *et al.* The role of surface oxygen in the growth of large single-crystal graphene on copper. *Science* **342**, 720–723 (2013).
3. Yan, Z. *et al.* Toward the synthesis of wafer-scale single-crystal graphene on copper foils. *ACS Nano* **6**, 9110–9117 (2012).
4. Bae, S. *et al.* Roll-to-roll production of 30-inch graphene films for transparent electrodes. *Nat. Nanotechnol.* **5**, 574–578 (2010).
5. Kobayashi, T. *et al.* Production of a 100-m-long high-quality graphene transparent conductive film by roll-to-roll chemical vapour deposition and transfer process. *Appl. Phys. Lett.* **102**, 1–5 (2013).
6. Li, X. *et al.* Graphene films with large domain size by a two-step chemical vapour deposition process. *Nano Lett.* **10**, 4328–4334 (2010).
7. Kim, H. *et al.* Activation energy paths for graphene nucleation and growth on Cu. *ACS Nano* **6**, 3614–3623 (2012).
8. Wang, Z.-J. *et al.* Direct observation of graphene growth and associated copper substrate dynamics by *in-situ* scanning electron microscopy. *ACS Nano* **9**, 1506–1519 (2015).
9. Li, X., Cai, W., Colombo, L. & Ruoff, R. S. Evolution of graphene growth on Ni and Cu by carbon isotope labeling. *Nano Lett.* **9**, 4268–4272 (2009).
10. Bhaviripudi, S., Jia, X., Dresselhaus, M. S. & Kong, J. Role of kinetic factors in chemical vapour deposition synthesis of uniform large area graphene using copper catalyst. *Nano Lett.* **10**, 4128–4133 (2010).
11. Lewis, A. M., Derby, B. & Kinloch, I. A. The influence of gas phase equilibria on the chemical vapour deposition of graphene. *ACS Nano* **7**, 3104–3117 (2013).
12. Celebi, K. *et al.* Evolutionary kinetics of graphene formation on copper. *Nano Lett.* **13**, 967–974 (2013).
13. Vlasiouk, I. *et al.* Graphene nucleation density on copper: fundamental role of background pressure. *J. Phys. Chem. C* **117**, 18919–18926 (2013).
14. Li, X. *et al.* Large-area synthesis of high-quality and uniform graphene films on copper foils. *Science* **324**, 1312–1314 (2009).
15. Vlasiouk, I. *et al.* Role of hydrogen in chemical vapour deposition growth of large single-crystal graphene. *ACS Nano* **5**, 6069–6076 (2011).
16. Liu, L. *et al.* High-yield chemical vapour deposition growth of high-quality large-area AB-stacked bilayer graphene. *ACS Nano* **6**, 8241–8249 (2012).
17. Wu, B. *et al.* Equiangular hexagon-shape-controlled synthesis of graphene on copper surface. *Adv. Mater.* **23**, 3522–3525 (2011).
18. Li, X. *et al.* Large-area graphene single crystals grown by low-pressure chemical vapour deposition of methane on copper. *J. Am. Chem. Soc.* **133**, 2816–2819 (2011).
19. Wu, B. *et al.* Self-organized graphene crystal patterns. *NPG Asia Mater.* **5**, e36 (2013).
20. Kidambi, P. R. *et al.* The parameter space of graphene chemical vapour deposition on polycrystalline Cu. *J. Phys. Chem. C* **116**, 22492–22501 (2012).
21. Zhang, Y. *et al.* Vapour trapping growth of single-crystalline graphene flowers: synthesis, morphology, and electronic properties. *Nano Lett.* **12**, 2810–2816 (2012).
22. Ma, T. *et al.* Edge-controlled growth and kinetics of single-crystal graphene domains by chemical vapour deposition. *Proc. Natl. Acad. Sci. USA* **110**, 20386–20391 (2013).
23. Zhao, P. *et al.* Role of hydrogen in oxygen-assisted chemical vapour deposition growth of millimeter-sized graphene single crystals. *Nanoscale* **8**, 7646–7653 (2016).
24. Zhou, H. *et al.* Chemical vapour deposition growth of large single crystals of monolayer and bilayer graphene. *Nat. Commun.* **4**, 1–8 (2013).
25. Gao, L. *et al.* Efficient growth of high-quality graphene films on Cu foils by ambient pressure chemical vapour deposition. *Appl. Phys. Lett.* **97**, 183109 (2010).
26. Yao, Y. *et al.* Controlled growth of multilayer, few-layer, and single-layer graphene on metal substrates. *J. Phys. Chem. C* **115**, 5232–5238 (2011).
27. Zhang, X., Wang, L., Xin, J. H., Yakobson, B. I. & Ding, F. Role of hydrogen in graphene chemical vapour deposition growth on a copper surface. *J. Am. Chem. Soc.* **136**, 3040–3047 (2014).
28. Chen, W. *et al.* Atomistic mechanisms for bilayer growth of graphene on metal substrates. *Phys. Rev. B* **91**, 045408 (2015).
29. Kawase, M., Ito, T. & Miura, K. *In-situ* infrared spectroscopy of hydrocarbons in a pyrocarbon CVD reactor. *ECS Trans.* **25**, 349–355 (2009).
30. Anderson, L. W., Goyette, A. N. & Lawler, J. E. Uses of high-sensitivity white-light absorption spectroscopy in chemical vapour deposition and plasma processing. *Adv. Atom. Mol. Opt. Phys.* **43**, 295–339 (2000).
31. Liu, W., Li, H., Xu, C., Khatami, Y. & Banerjee, K. Synthesis of high-quality monolayer and bilayer graphene on copper using chemical vapour deposition. *Carbon* **49**, 4122–4130 (2011).
32. Xing, S., Wu, W., Wang, Y., Bao, J. & Pei, S.-S. Kinetic study of graphene growth: Temperature perspective on growth rate and film thickness by chemical vapor deposition. *Chem. Phys. Lett.* **580**, 62–66 (2013).
33. NIST X-ray Photoelectron Spectroscopy Database, Version 4.1 (National Institute of Standards and Technology, Gaithersburg); <http://srdata.nist.gov/xps/> (2012).
34. Verguts, K. *et al.* Epitaxial Al₂O₃(0001)/Cu(111) template development for CVD graphene growth. *J. Phys. Chem. C* **120**, 297–304 (2016).
35. Holland, L. Vacua: how they may be improved or impaired by vacuum pumps and traps. *Vacuum* **21**, 45–53 (1971).
36. Holland, L., Steckelmacher, W. & Yarwood, J. *Vacuum Manual*. (E. & F.N. Spon, 1974).
37. Hablani, M. H., Bez, E. & Farrant, J. L. Elimination of backstreaming from mechanical vacuum pumps. *J. Vac. Sc. Technol. A* **5**, 2612–2615 (1987).
38. Laurenson, L., Hickman, S. & Livesey, R. G. Rotary pump backstreaming: an analytical appraisal of practical results and the factors affecting them. *J. Vac. Sc. Technol. A* **6**, 238–242 (1988).
39. O'Hanlon, J. F. *A user's guide to vacuum technology*. (John Wiley & Sons Inc., 2004).

40. Jones, A. C. & Hitchman, M. L. *Chemical vapour deposition: precursors, processes, and applications*. (Royal Society of Chemistry, 2009).
41. Fulker, M. J. Backstreaming from rotary pumps. *Vacuum* **18**, 445–449 (1968).
42. Suzuki, S., Nagamori, T., Matsuoka, Y. & Yoshimura, M. Threefold atmospheric-pressure annealing for suppressing graphene nucleation on copper in chemical vapour deposition. *Jpn. J. Appl. Phys.* **53**, 095101 (2014).
43. Vlassiok, I. *et al.* Large scale atmospheric pressure chemical vapour deposition of graphene. *Carbon* **54**, 58–67 (2013).
44. Ghosh, P. *et al.* Insights on defect-mediated heterogeneous nucleation of graphene on copper. *J. Phys. Chem. C* **119**, 2513–2522 (2015).
45. Trinsoutrot, P. *et al.* The role of the gas phase in graphene formation by CVD on copper. *Chem. Vap. Depos.* **20**, 51–58 (2014).
46. Li, G., Huang, S.-H. & Li, Z. Gas-phase dynamics in graphene growth by chemical vapour deposition. *Phys. Chem. Chem. Phys.* **17**, 22832–22836 (2015).
47. Li, Z. *et al.* Graphene thickness control via gas-phase dynamics in chemical vapour deposition. *J. Phys. Chem. C* **116**, 10557–10562 (2012).
48. Li, Q. *et al.* Growth of adlayer graphene on Cu studied by carbon isotope labeling. *Nano Lett.* **13**, 486–490 (2013).
49. Yu, H. K. *et al.* Chemical vapour deposition of graphene on a ‘peeled-off’ epitaxial Cu (111) foil: a simple approach to improved properties. *ACS Nano* **8**, 8636–8643 (2014).
50. Procházka, P. *et al.* Ultrasoother metallic foils for growth of high quality graphene by chemical vapour deposition. *Nanotechnology* **25**, 185601 (2014).

Acknowledgements

We acknowledge the support from the EU Seventh Framework Programme (FP7/2007–2013) under grant agreement number FP7-604007 “GLADIATOR” and the EC Graphene FET Flagship, grant agreement number 604391, and the Danish National Research Foundation Center of Excellence for Nanostructured Graphene (CNG), project DNRF103.

Author Contributions

A.S. conceived the experiments. A.S. designed the experiments and performed the measurements. P.B., T.B. and O.H. assisted in the analysis and interpretation of UV absorption results. D.M. and B.L. assisted in data analysis. A.S. and T.B. prepared the manuscript and all figures. D.M. assisted with preparation of figures. All authors discussed the results and commented on the manuscript.

Additional Information

Supplementary information accompanies this paper at doi:10.1038/s41598-017-06276-y

Competing Interests: The authors declare that they have no competing interests.

Publisher's note: Springer Nature remains neutral with regard to jurisdictional claims in published maps and institutional affiliations.



Open Access This article is licensed under a Creative Commons Attribution 4.0 International License, which permits use, sharing, adaptation, distribution and reproduction in any medium or format, as long as you give appropriate credit to the original author(s) and the source, provide a link to the Creative Commons license, and indicate if changes were made. The images or other third party material in this article are included in the article's Creative Commons license, unless indicated otherwise in a credit line to the material. If material is not included in the article's Creative Commons license and your intended use is not permitted by statutory regulation or exceeds the permitted use, you will need to obtain permission directly from the copyright holder. To view a copy of this license, visit <http://creativecommons.org/licenses/by/4.0/>.

© The Author(s) 2017